

Interannual Sea Surface Temperature Variability and the Predictability of Tropical Intraseasonal Variability

DUANE E. WALISER AND ZHENZHOU ZHANG

Institute for Terrestrial and Planetary Atmospheres, State University of New York at Stony Brook, Stony Brook, New York

K. M. LAU

Climate and Radiation Branch, NASA Goddard Space Flight Center, Greenbelt, Maryland

JAE-HOON KIM

Space Applications Corporation, Vienna, Virginia

(Manuscript received 15 December 1999, in final form 26 January 2001)

ABSTRACT

The objective of this study is to examine the relationship between interannual SST variability and the activity and predictability of tropical intraseasonal variability (TISV). A 10-yr simulation forced by climatological SSTs and a 10-member 10-yr (1979–88) ensemble of simulations forced by observed SSTs from the NASA Goddard Laboratory for the Atmospheres GCM coupled to a weakly interacting slab ocean mixed layer are analyzed. The climatological simulation provides a measure of the natural variability associated with TISV, while the observed SST simulations provide an indication of how externally imposed SST anomalies modify this variability. Analysis is conducted on both the eastward-propagating (winter mode) and northeastward-propagating (summer mode) forms of TISV. Indices of TISV are constructed from the amplitude time series of the leading EOFs of intraseasonally bandpassed model precipitation and 850-hPa zonal wind. Analysis of the TISV activity indices from the climatological SST simulation shows that considerable natural variability exists for both the winter and summer TISV modes. Based on the TISV indices constructed, the internal variability of TISV is about 50% of the mean signal. Moreover, the interannual standard deviation in TISV activity from the climatological SST simulation ranges from about the same size to about twice the standard deviation associated with the seasonal evolution of TISV activity.

A ratio between an estimate of the externally forced TISV variability in the observed SST simulations to an estimate of natural TISV variability from the climatological SST simulations is constructed to give a measure of TISV predictability. While these predictability values exhibit some seasonal dependence, on average they suggest little to no predictability associated with interannual TISV variations for either the winter or summer TISV mode. However, the ensemble does demonstrate significantly enhanced predictability of the summer TISV mode during the 1982/83 winter. This same characteristic was found during the 1997/98 winter in a second 10-member ensemble that was conducted for the period September 1996 to August 1998. In each of these cases, the ensemble means exhibited a decrease in TISV activity, a feature that is also echoed in the observations. Thus, under very specific circumstances, anomalous SST may have some predictable influence over the level of TISV activity, at least for the summer mode. In addition, the simulations show evidence that generalized intraseasonal variance (i.e., no constraint on spatial structure) displays some predictable characteristics over the central and eastern equatorial Pacific in association with ENSO-related SST anomalies.

Considerations of the use of the ocean mixed layer coupling in the context of the above study are discussed as well as the agreement between the observed levels of TISV activity for the periods modeled and the levels simulated by the GCM ensemble.

1. Introduction

Tropical intraseasonal variability (TISV) takes on a number of forms, one of which was first identified in

the early seventies and has since been widely referred to as the Madden–Julian oscillation (MJO; Madden and Julian 1971, 1972). These large-scale tropical disturbances are characterized by eastward-propagating, equatorially trapped, baroclinic oscillations in the tropical wind field (Madden and Julian 1994; Hendon and Salby 1994). Over the warmest tropical waters, such as the Indian and west Pacific Oceans, there is considerable interaction between these wind field oscillations and

Corresponding author address: Duane E. Waliser, Institute for Terrestrial and Planetary Atmospheres, State University of New York, Endeavour Hall 205, Stony Brook, NY 11794-5000.
E-mail: waliser@terra.msfc.sunysb.edu

anomalies in atmospheric deep convection. In these regions, where the convective coupling is strong, the oscillation propagates rather slowly, about $5\text{--}10\text{ m s}^{-1}$. Once the disturbances reach the vicinity of the date line, and thus cooler equatorial waters, the convection subsides and the propagation speed increases to about $15\text{--}20\text{ m s}^{-1}$ or greater. Several studies suggest that the MJO propagates slowly during its convective phase due to a coupling between Kelvin and Rossby waves brought about by the strong latent heating (e.g., Wang and Rui 1990a; Salby et al. 1994) as well as a tighter coupling to the underlying warm SST (e.g., Wang and Xie 1998; Waliser et al. 1999b). In the Western Hemisphere, where the convective coupling is weak, the MJO behaves much like a damped Kelvin wave, and the phase speed is considerably faster. The above characteristics tend to be most strongly exhibited during the boreal winter and spring when the Indo-Pacific warm pool is centered at or near the equator. In addition to this eastward-moving, equatorially trapped form of TISV, there are other forms that propagate poleward from the equatorial Indian Ocean into Southeast Asia during the Northern Hemisphere summer and into northern Australia during Southern Hemisphere summer (e.g., Lau and Chan 1986; Wang and Rui 1990b). These poleward propagating forms account for about half of all the large-scale, propagating intraseasonal events in the Tropics (Wang and Rui 1990b).

Interest in TISV has become more widespread in recent years due to the extensive interactions TISV has with other components of our climate system. For example, one of the most distinct features of the Asian–Australian monsoon is its sudden onsets and breaks. Observations have revealed that monsoon onset and breaks are closely related to poleward-propagating TISV activity (e.g., Yasunari 1980; Lau and Chan 1986; Hendon and Liebmann 1990a,b; Webster et al. 1998). In addition to having an influence over the seasonal timescale, at times there appears to be a connection between eastward-propagating MJO events and the timing and evolution of El Niño events. This connection results from the fact that strong westerly surface winds accompany MJO convective activity. When MJO disturbances reach the Pacific Ocean, these westerly winds initiate downwelling oceanic Kelvin waves that can lead to SST warming in the east Pacific due to a suppression of the local thermocline (e.g., Lau and Chan 1988; Zebiak 1989; Weickmann 1991; Kessler et al. 1995; Moore and Kleeman 1999). The recent 1997/98 El Niño appears to be a particularly illustrative example of the interaction between MJO-related surface wind forcing and the development of an El Niño (McPhaden 1999). In this same context, there is even an indication that intraseasonal forcing may impart a nontrivial influence on the mean state of the western Pacific Ocean (Kessler and Kleeman 2000). Finally, besides the interactions between TISV and longer timescale variability, many studies have shown an influence from TISV on the extratropical cir-

ulation and its associated weather patterns (e.g., Weickmann 1983; Liebmann and Hartman 1984; Weickmann et al. 1985; Lau and Philips 1986; Higgins and Mo 1997). In fact, numerical weather prediction experiments by Ferranti et al. (1990) suggest that skill scores for Northern Hemisphere long-range weather forecasts can be improved if the Tropical diabatic heating related to the MJO is well simulated/predicted (cf., Waliser et al. 1999a; Hendon et al. 2000; Jones et al. 2000).

Along with the seasonal modulation of TISV activity described above, there is also substantial interannual variability in its intensity (e.g., Lau and Chan 1988; Salby and Hendon 1994; Fink and Speth 1997). From observational studies such as these, the question arises: Is this interannual behavior of TISV purely chaotic and unpredictable or is it related to the slowly changing boundary forcing (e.g., SST) and therefore potentially predictable on seasonal to interannual timescales? Observational studies such as that by Hendon et al. (1999; see their Fig. 5) show that while both Northern Hemisphere winter TISV activity (i.e., MJO) and eastern Pacific Ocean SST anomalies each undergo significant interannual variability, it is not obvious that the intensity of their variations are related. Thus, while there does not appear to be much evidence for a strong link between this form of TISV and anomalous SST in the eastern Pacific Ocean, it is possible that SST in other regions of the ocean may influence the interannual character of TISV, or that other measures of TISV activity (e.g., poleward-propagating TISV) might be more closely connected to ENSO-related SST variability.

The only studies to date addressing the above question concerning overall interannual predictability of TISV as it relates to interannual SST anomalies are those by Slingo et al. (1999) and Gualdi et al. (1999). In the former, a four-member ensemble of 45-yr simulations with the Met Office (UKMO) general circulation model (GCM; i.e., HADAM2a) was analyzed, while in the latter a 15-member ensemble of 14-yr simulations with the ECHAM4 GCM was analyzed. Each study employed observed SST surface boundary conditions. Further each study focused on the average reproducibility of the interannual character of TISV in their ensembles with a focus on the Northern Hemisphere winter “form” of TISV (i.e., the eastward, equatorially propagating form). For the most part, each study concluded that there was little reproducibility in interannual TISV variability associated with anomalous SST. However, closer examination of their results (e.g., Fig. 11 in Slingo et al. 1999), indicates that some years did appear to show similarity amongst the ensemble members. Does this imply that there is predictability under certain anomalous conditions and/or certain TISV modes? In addition, how dependent are these studies conclusions regarding predictability on the seasonal “form” of the TISV (i.e., poleward versus equatorially propagating modes)? Finally, just as the simulation characteristics of TISV are strongly model dependent (e.g., Slingo et al. 1996), as

well as dependent on the nature of the SST boundary condition (e.g., Waliser et al. 1999b), it is possible that conclusions regarding TISV predictability might also be model framework dependent, and therefore need to be examined with a number of GCMs whose simulation characteristics of TISV appear relatively realistic.

The objective of this study is to examine the interannual predictability of TISV with a different atmospheric GCM, a different experimental setup, and a slightly broader focus than that used in the Slingo et al. (1999) and Gualdi et al. (1999) studies. Briefly, the experiments and analysis undertaken in this study complement those two studies in four ways. First, this study uses the National Atmospheric and Space Administration (NASA) Goddard Laboratory for the Atmospheres (GLA) GCM, which along with the UKMO and ECHAM4 model is also known to provide a good representation of the MJO (see section 2). Second, the numerical experiments include a weakly coupled SST that provides a more realistic surface boundary condition than the fixed SSTs used by Slingo et al. (1999) and Gualdi et al. (1999). Third, the analysis will examine the seasonal dependence and temporal variability of TISV predictability, including the latter's relation to interannual SST anomalies, as well as put the assessment of predictability in the context of an estimate of natural variability. Finally, this analysis will include an assessment of the predictability of TISV in general, that is, that which is not constrained by a predefined spatial-temporal organization.

In the next section, the NASA GLA GCM is described along with the experimental design and preliminary analysis methods. Section 3 describes the procedures used to quantify TISV activity and applies them to the simulation using climatological SSTs in order to assess the natural variability associated with TISV. Section 4 describes the TISV in the ensemble of simulations using observed SSTs, compares it to the natural variability found in the simulation using climatological SSTs, and examines to what degree the large-scale interannual SST anomalies influence TISV predictability. In addition, analysis in section 4 explores the predictability of generalized intraseasonal variability, meaning TISV that is not necessarily associated with a given large-scale coherent structure (e.g., the MJO). Further discussion and a summary are presented in section 5.

2. Model and experiments

The model used in these experiments is the GLA GCM. This model was derived from an earlier version described by Kalnay et al. (1983). Modifications have included increased vertical resolution and several changes in the parameterizations of radiation, convection, cloud formation, precipitation, vertical diffusion, and surface processes (Sud and Walker 1992; Phillips 1996). The horizontal representation uses surface finite differences on a $4^\circ \text{ lat} \times 5^\circ \text{ long}$ energy and momentum

conserving A grid (Arakawa and Lamb 1977). The horizontal advection of the atmospheric variables is accurate to fourth order (Kalnay et al. 1983). The vertical domain has 17 unequally spaced sigma levels extending from the surface to about 12 hPa. At every dynamical time step, a 16-order Shapiro (1970) filter (with time-scale 90 min) is applied to the prognostic fields; a Fourier filter is also used in polar latitudes. Negative moisture values are filled by "borrowing" moisture from the level below, and from neighboring horizontal grid boxes at the lowest vertical level. Horizontal diffusion is not included and the effects of vertical diffusion are treated by the level-2.5 second-order turbulence closure model of Helfand and Labraga (1988). Near the surface, the planetary boundary layer is treated as an extended surface layer with a viscous sublayer in the space between the surface and the tops of the surface roughness elements. Appropriate parameterizations are utilized to determine turbulent fluxes in the different planetary boundary layer subregions. Both seasonal and diurnal cycles in the solar forcing are simulated with the atmospheric radiation treatment of Harshvardhan et al. (1987). The formulation of the convection follows the scheme of Arakawa and Schubert (1974), as implemented in discrete form by Lord and Arakawa (1980). The model orography is based on the $1^\circ \times 10^\circ$ topographic height data of Gates and Nelson (1975), which has been area-averaged over the 40×50 grid boxes. The resulting orography is smoothed using a 16-order Shapiro (1970) filter, and a Fourier filter poleward of 60° latitude. Negative terrain heights resulting from the smoothing process are set to zero. Land surface processes are simulated as in the Xue et al. (1991) modification of the model of Sellers et al. (1986).

In general, the GLA model performed very well with respect to its representation of the MJO (i.e., the eastward, equatorially propagating mode) in the Slingo et al. (1996) Atmospheric Model Intercomparison Project (AMIP) study, being one of about three models [UKMO, GLA, and the National Center for Atmospheric Research Community Climate Model version 2 (CCM2)] that contained variability closely resembling the observed features of the oscillation. In fact, a more rigorous comparison of the MJO in the GLA and UKMO models by Sperber et al. (1996) showed that of the two models, the GLA model tended to produce a better representation of the eastward propagation of convection and its associated cyclonic and anticyclonic circulation anomalies. To date, there has not been a systematic model comparison of the simulation characteristics of the northeastward propagating form of TISV, the form that plays an important role in the evolution of the Asian summer monsoon. Therefore, the results regarding Northern Hemisphere summertime TISV should be regarded with a bit more caution than those associated with the wintertime TISV.

Improvements in the GLA simulation of the MJO relative to observed characteristics and the typical mod-

el shortcomings identified by Slingo et al. (1996) were made by Waliser et al. (1999b) by incorporating the coupled SST feedback from a simple slab ocean mixed layer. These improvements included an increase in the intensity of the simulated MJO variability, a reduced propagation speed of the MJO in the Eastern Hemisphere, and an increase in the seasonality of the MJO signal. Therefore, in order to have the most realistic simulation of the MJO (and presumably TISV in general) afforded by the GLA GCM, the slab ocean mixed layer coupling is included in the simulations performed for this study. Briefly, this model is described by

$$\frac{dT'}{dt} = \frac{F'}{\rho C_p H} - \gamma T', \quad (1)$$

where T' is the SST anomaly, F' is the net surface flux anomaly, H is a fixed mixed layer depth, γ is a damping factor, ρ is the density of water, and C_p is the specific heat of water. The slab model is only applied equatorward of 20° . The net surface flux climatology (12-month annual cycle) used to compute the flux anomalies is taken from a simulation using specified climatological SSTs without the ocean model. The damping factor is meant to keep the model climate relatively close to its uncoupled mean climatology and to account for neglected terms (e.g., ocean advection and turbulence mixing). In the simulation presented here, γ is set to $1/(50$ days). The mixed layer depth H is taken to be 50 m. Both H and γ were set relatively conservatively in order that the SST anomalies only represent a modest perturbation. Note that the mixed layer model is only intended to provide a high-frequency SST anomaly that is coupled with the evolution of the atmosphere. This anomaly is added to the background SST field, which is specified from either climatology or observations. For further details on the slab mixed layer, the motivation for its specification, and the impact it has on the simulation of TISV, see Waliser et al. (1999b).

In this study, ten 10-yr simulations using observed SSTs from 1979 to 1988 and one 10-yr simulation using climatological SSTs were performed. The climatological SST simulation is used to assess the natural variability of TISV, that is, that part that is not associated with interannual variations in SST. The 10 simulations using observed SSTs differed in their initial conditions, and will be referred to as the observed or ensemble simulations. The nine additional initial conditions used for the observed SST simulations came from the day 6, 11, 16, 21, etc., atmospheric states of the climatological SST simulation. The statistical behavior of TISV in the observed SST simulations will be compared to the variability in the climatological SST simulation in order to assess the predictability of TISV associated with the interannual variability of SST.

It is important to recognize that when implementing the slab ocean model in the climatological SST case, the SST perturbations tend to be small and short-lived

due to the damping term and due to the fact that the heat flux climatology used in its implementation comes from a climatological simulation. However, when it is applied to simulations employing observed SSTs, the SST perturbations can become somewhat larger and longer-lived since significant interannual flux anomalies develop in these simulations (e.g., due to El Niño). This ends up presenting a bit of a trade-off of desirable features in the experimental setup for assessing predictability. On one hand, it is highly desirable to have the most realistic representation of the MJO, which necessarily includes an interactive SST. On the other hand, the SST for the 10 ensemble simulations is not exactly identical, which is often what is desired when separating internal from SST-forced variability. However, examination of the SST from the 10 simulations shows that the intraensemble SST variability resulting from the interactive SST scheme is relatively small compared to the interannual SST variability in the observations. Thus, all 10 observed SST simulations still "see" generally the same interannually varying SST field, but each develops minor SST variations around this value. This aspect of the study will be discussed further in the summary section.

In addition to the simulations described above, a 10-member ensemble of 2-yr (September 1996–August 1998) simulations is employed to provide supplementary support for one aspect of the analysis. This ensemble was performed as part of the World Climate Research Program–Climate Variability and Predictability (WCRP–CLIVAR) Asian–Australian Monsoon Atmospheric GCM Intercomparison Project. The only differences in the experimental setup between this ensemble and that described above are this ensemble used weekly rather than monthly SSTs from observations and, to be consistent with other participating modeling groups, it did not employ the slab ocean coupling. Thus the characteristics of the MJO will be somewhat different between these two cases. However, in terms of the amount of intraseasonal variability, the two differences introduced would expect to cancel out to some extent, since the omission of the slab will reduce the amount of variability and the use of weekly versus monthly SSTs will likely increase the variability (Wei et al. 2001).

While TISV is readily identifiable in many meteorological variables, including near-surface zonal wind, sea level pressure, upper-level zonal wind, precipitation, outgoing longwave radiation, etc., this study analyzes TISV activity based on the 850-hPa zonal wind (hereafter U850) and precipitation. This choice was motivated by having one dynamic and one hydrological variable to depict TISV variability. Since we are primarily interested in intraseasonal variability in the tropics, the analysis domain was limited to the region between 30°N and 30°S . To further reduce the computation expense for this study, the 6-h output of the model simulations were averaged to 5-day means (pentads), with each year

having exactly 73 pentads. In order to isolate the intra-seasonal timescale, the data were filtered with a 20–100-day Lanczos bandpass filter (Duchon 1979). The sensitivity of the results to this choice of intraseasonal frequency window will be assessed through the discussion of a parallel analysis with a narrower window of 35–70 days.

3. Natural variability of TISV

a. EOF analysis: Spatial variability

As discussed in the introduction, TISV exhibits a strong seasonal dependence. In the boreal winter/spring, TISV tends to propagate eastward along the equator, while in the boreal summer, TISV tends to propagate northeastward into Southeast Asia. Therefore it is reasonable to analyze the variability of TISV taking into account this seasonal dependence. To do so, the filtered data is divided into “winter” and “summer” seasons (with respect to the Northern Hemisphere). The summer season is defined from May to October and the winter season is defined from November to April. From these data, empirical orthogonal function (EOF) analysis is used to capture the dominant spatial structure of TISV for each season. This analysis was performed on all 11 simulations together (i.e., 10 observed SST and one climatological SST). Since a subset of the resulting EOF modes will be used later in the construction of a TISV activity index, this was done so that the character of the TISV in each simulation was weighted equally in the EOF analysis.

Figure 1 shows the first two EOF modes of U850 (top) and precipitation (bottom) for the winter season. In general, these two pairs of eigenvectors represent the large-scale salient features of the eastward equatorially propagating form of TISV (cf. Murakami et al. 1986; Ferranti et al. 1990). The amplitude time series of these EOF pairs have correlations of about ± 0.5 at lags of ± 2 pentads, implying about a 40-day timescale. In the case of the precipitation vectors, the regions of maximum anomaly are almost exclusively limited to the near-equatorial regions of the Indian and western/central Pacific Oceans. The combination of the two modes depicts an eastward evolving heat source that starts in the central Indian Ocean, appears to diminish over the maritime continent, amplifies over the western Pacific, then decays as it moves southeastward into the region associated with the South Pacific convergence zone. The first EOF mode (Fig. 1c) accounts for about 4.4% of the anomaly bandpassed variance, and has a maximum value of 5 mm day^{-1} . The second mode (Fig. 1d) accounts for 3.7% of the anomaly bandpassed variance, and also has a maximum value of about 5 mm day^{-1} . These are sizeable perturbations, given that the model (and observed) mean rainfall rates in the tropics are on the order of $5\text{--}10 \text{ mm day}^{-1}$ (see Fig. 1 of Waliser et al. 1999b). In the case of the lower-level winds, the spatial structure

also shows considerable symmetry with respect to the equator with most variability confined between the Indian Ocean and the central Pacific Ocean. The first EOF mode (Fig. 1a) accounts for 7.1% of the bandpassed anomaly variance with a maximum value of about 2.5 m s^{-1} . When considered in conjunction with a negative amplitude coefficient, the anomaly is roughly consistent with diabatic heating centered over the western Pacific Ocean, and the positive wind perturbation west of the heating would be the so-called westerly wind burst that is associated with the MJO. The second EOF mode (Fig. 1b) accounts for 6.3% of the bandpassed anomaly variance and it has a maximum value of about 3 m s^{-1} . In this case, the negative of its spatial structure is roughly consistent with diabatic heating centered over the Indian Ocean. Together these two pairs of EOF modes, which are often taken to represent the MJO, will be referred to in this study as the “winter mode” of TISV.

Figure 2 shows the same results but for the summer season. In contrast to the winter case, these modes show virtually no symmetry with respect to the equator. Taken together, the two precipitation vectors depict a northeastward propagating movement of diabatic heating from the eastern Indian Ocean, past Southeast Asia, and into the western subtropical Pacific. As discussed in the introduction, this sort of summertime TISV is strongly related to the onset and breaks of the Southeast Asian summer monsoon. The first mode (Fig. 2c) explains 4.7% of the variance, while the second mode (Fig. 2d) explains 4.2%, and each has maximum anomaly values of about 5 mm day^{-1} . The U850 eigenvectors depict a similar pattern of migrating variability, with variations on the order of $3\text{--}4 \text{ m s}^{-1}$. The first mode (Fig. 2a) accounts for 7.3% of the bandpassed anomaly variance, while the second mode accounts for 6.7%. Together these two pairs of EOF modes will be referred to as the “summer mode” of TISV.

While the variance percentages of the above EOF modes seem quite small, they are based on analyses of roughly 1152 grid points (16×72) and 8030 pentads (11×730). Since the number of spatial grid points is less than the number of time points, there are a total of 1152 EOF modes resulting from the analysis. If the variance was spread equally among this number, each mode would have approximately 0.09%. Since the first two EOFs in both the winter and summer seasons is about a hundred times this amount, these patterns in fact do represent dominant modes of variability within the data. This is further evident in Fig. 3, which shows the variance percentages of the U850 and precipitation EOFs for both summer and winter. Evident is the rather sharp drop in variance after mode 2, especially for U850. While the analysis presented below focuses mainly on the first two modes, the sensitivity of the results to this choice for the number of modes to retain will be assessed through the discussion of parallel analyses using additional modes.

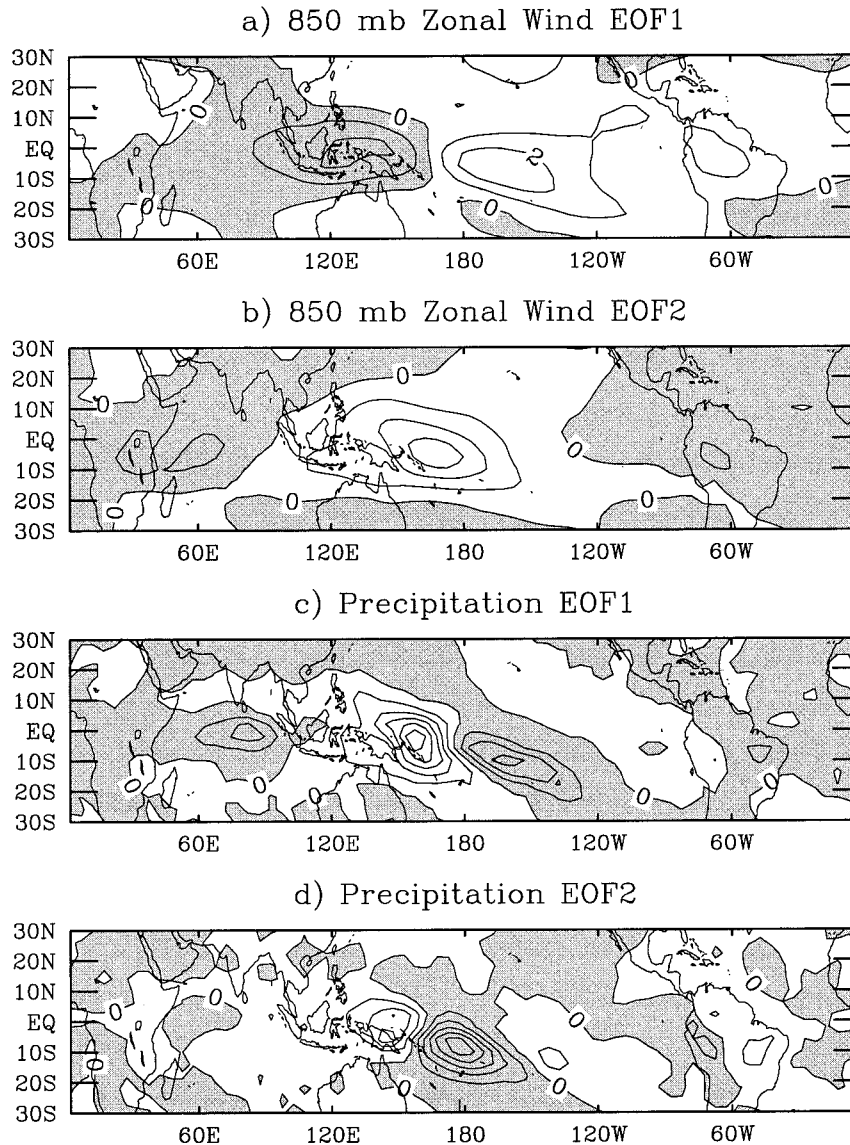


FIG. 1. (a) First and (b) second leading EOF spatial patterns for 850-hPa zonal wind generated from the combined, intraseasonally bandpassed output of the climatological SST and the 10 observed SST simulations for the Northern Hemisphere "winter" season (defined as Nov–Apr). (c) and (d) The same except for precipitation.

b. TISV activity index: Temporal variability

In order to assess the interannual variations of TISV, it is necessary to construct a measure of TISV temporal variability. Since the first few bandpassed EOFs represent a sizable fraction of the variance associated with the canonical TISV for a given season, a rather robust index of TISV activity can be computed from the sum of the eigenvalue-weighted EOF amplitude time series as follows: (Ferranti et al. 1990; Slingo et al. 1999; Hendon et al. 1999):

$$\text{TISV_Activity_Index} = X(t) = \sqrt{\frac{1}{L} \sum_{i=1}^L \omega_i A_i(t)^2}, \quad (2)$$

where the ω_i is the eigenvalue of mode i , and $A_i(t)$ is the unit normalized amplitude time series of mode i . The latter is obtained by projecting a given variable's and season's mode i EOF pattern onto the bandpassed anomaly data from a given simulation. Here L represents the number of modes to be kept in the representation of TISV. Given that the first two modes are enough to represent the propagating and canonical nature of the TISV activity being investigated, L is set equal to 2. This choice is consistent with the indices constructed by Ferranti et al. (1990) and Hendon et al. (1999). As mentioned above, the sensitivity of the results to this particular cutoff will be addressed by discussing results

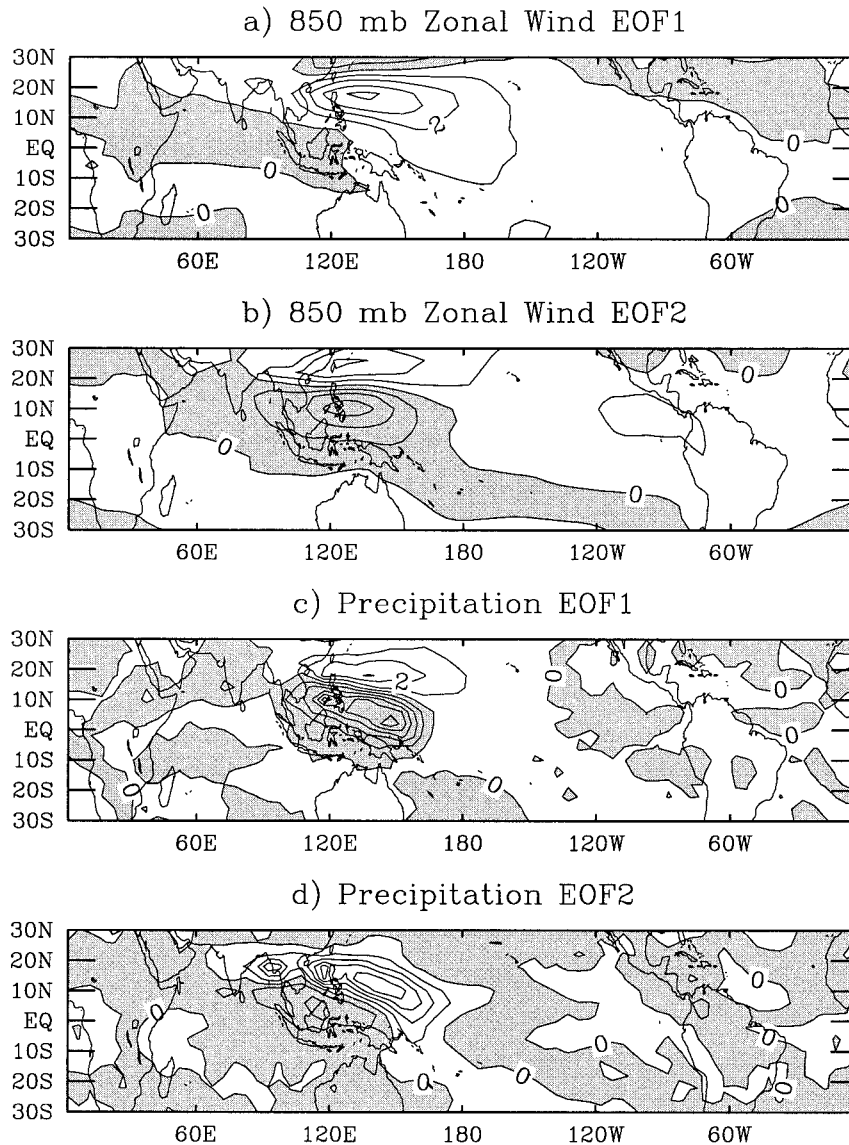


FIG. 2. Same as Fig. 1 except for the summer season (defined as May–Oct).

obtained by setting L equal to 9. The above scheme results in a 730-pentad (i.e., 10 yr) time series depicting a measure of the TISV activity associated with that variable and TISV mode. Naturally, since the summer modes highlight the typical structure of TISV in that “season,” the activity index computed from summer EOFs will tend to have larger amplitudes in summer than winter, and vice versa for the winter modes. Using the above formulation, separate TISV indices can be computed for each variable and each TISV mode from each model simulation.

To illustrate and describe the TISV in the climatological SST simulation, the above TISV activity indices were computed from the output of this simulation for both precipitation and U850 and for both winter and summer seasons. The resulting 10-yr time series were

then split into ten 1-yr time series according to calendar year. Assuming the TISV activity index for a given variable and mode from the climatological run is represented as X_{ij}^C , where i represents year from 1 to N ($=10$), j represents pentad from 1 to 73, and C denotes climatological SSTs, the means and standard deviations of these series were calculated as follows:

$$\langle X^C \rangle_j = \frac{1}{N} \sum_{i=1}^N X_{ij}^C, \quad (3)$$

$$\sigma_j^{C2} = \frac{1}{N-1} \sum_{i=1}^N (X_{ij}^C - \langle X^C \rangle_j)^2. \quad (4)$$

The results of these calculations are shown in Fig. 4. In each plot, the solid thick line is the mean ($\langle X^C \rangle_j$), while the shading and thin dotted line both denote the

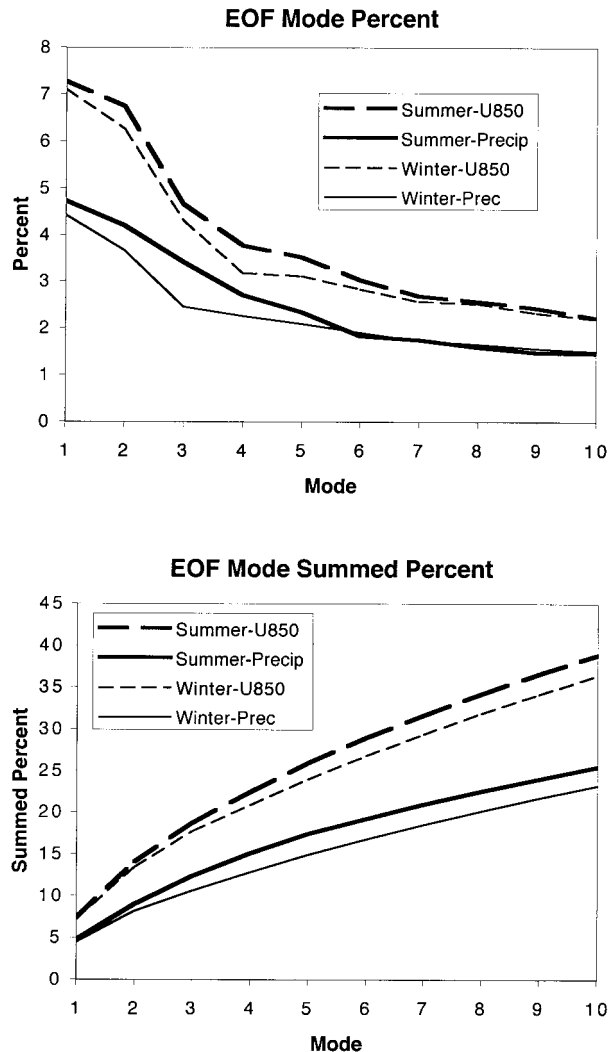


FIG. 3. (top) Percent variance of leading U850 (dotted) and precipitation (solid) EOFs for both the winter (thin) and summer (thick) TISV modes. (bottom) Running sum of percent variance of leading U850 (dotted) and precipitation (solid) EOFs for both the winter (thin) and summer (thick) TISV modes.

standard deviation (σ_f^c). Note that because these indices were computed from the climatological SST simulation, the variability displayed can be ascribed to purely natural, or internal, intraseasonal variability. As expected, the mean activity associated with the winter mode of TISV (Figs. 4a and 4b) tends to peak from December through February, while that for the summer mode of TISV (Figs. 4c and 4d) tends to peak from June through August. This difference is slightly more accentuated in the plots associated with precipitation. Overall, the mean values for these TISV indices range from about 0.5 during the period of the year when the given seasonal mode is strongly exhibited to about 1.0 during the period of the year when the given seasonal mode is not strongly exhibited. Note that these mean values indicate the typ-

ical amplitude that is found for the associated EOF patterns (i.e., Figs. 1 and 2) and thus give an approximate size of the typical TISV-related perturbation for that field during a given period of the calendar year.

The standard deviations (σ_f^c) presented in Fig. 4 give an indication of the reproducibility of the mean seasonal evolution from year to year in the climate simulation. Typically, these variations are on the order of 0.5, and thus relatively high compared to the mean values. This indicates that there is significant interannual variability in the TISV independent of any interannual variations of SST, and thus that the natural or internal variability of TISV is considerable. Slingo and Madden (1991) noted a similar finding in a perpetual January simulation of the NCAR CCM1 model. In fact, as measured by the indices constructed here, the interannual standard deviations (i.e., $\sigma_f^c \sim 0.25\text{--}0.5$) range from about the same size to about twice the size of the standard deviation of the mean seasonal evolution (~ 0.25). In addition, the typical interannual fluctuations (σ_f^c) associated with internal variability are about half the size of the mean levels of MJO activity ($\langle X^c \rangle$). The variations exhibited in the size of the standard deviations stem from the seasonal dependence of the mean values, and as expected are higher when the mean TISV values are higher. This is especially the case with the TISV indices associated with precipitation. In an absolute sense, this characteristic would indicate that there is less year-to-year reproducibility when the TISV activity is high. However, this consideration of predictability/reproducibility should only be made relative to a given time of year, as will be done in the next section when analyzing the observed SST simulations.

4. Variability of the TISV associated with observed SSTs

The results in the previous section showed that independent of any large-scale SST anomalies, there are significant year-to-year fluctuations in the intensity of TISV for both the winter and summer TISV modes. In this section, the interannual variability of TISV in the ensemble of simulations forced by observed SSTs will be analyzed to determine how these interannually varying boundary conditions influence the year-to-year TISV activity levels and their intraensemble variations.

a. Climatological TISV activity and predictability

In order to assess the interannual variability of TISV activity in the observed SST simulations, the TISV indices defined in the previous section were computed for each of the simulations of the 10-member ensemble. Similar to the previous section (i.e., Fig. 4), the mean values of the indices for all 10 simulations, along with the associated standard deviations, were computed for each year of the simulation period (1979–88). In this case,

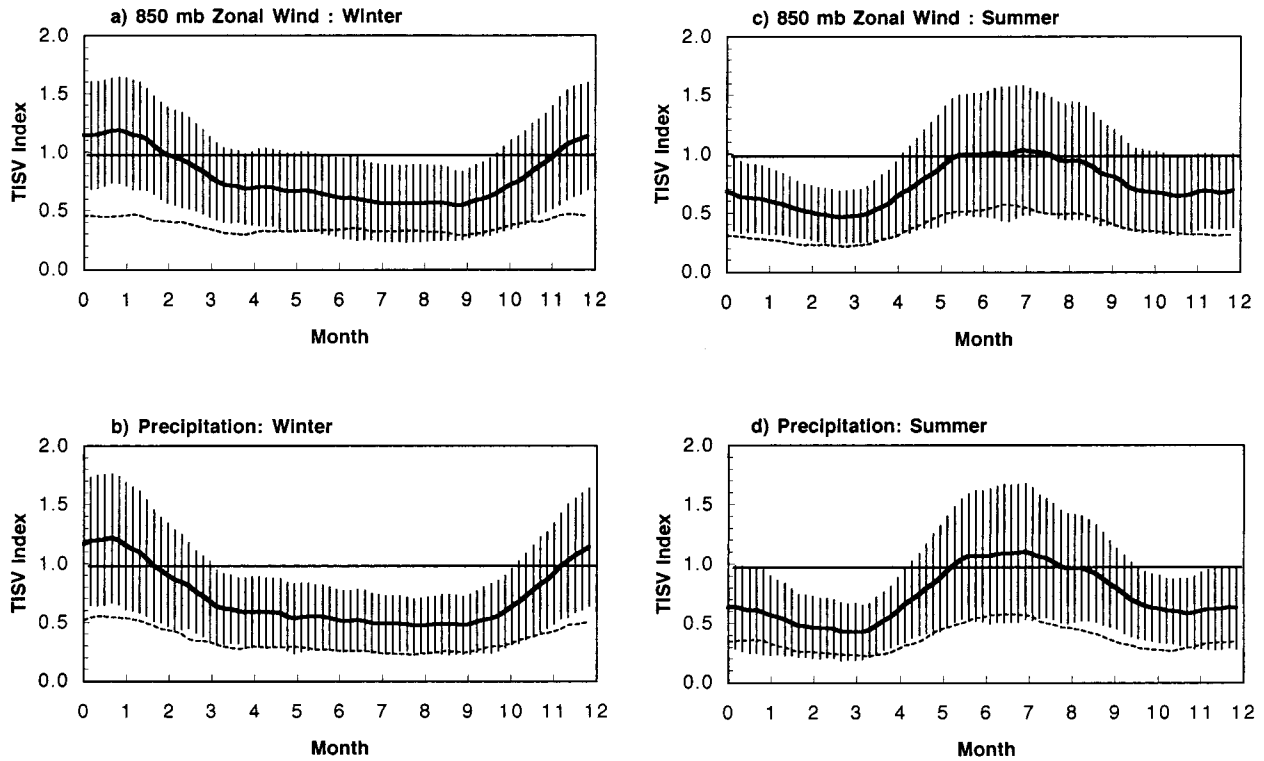


FIG. 4. Climatological (10-yr) mean (solid; $\langle X^c \rangle$) and standard deviation (dashed and shading; σ_f^c) TISV activity from the climatological SST simulation for (a) U850 winter, (b) precipitation winter, (c) U850 summer, and (d) precipitation summer TISV modes. Curves have been smoothed using a 15-pentad running mean filter. See section 3 for definitions of seasons and TISV activity index.

$$\langle X^o \rangle_{ij} = \frac{1}{M} \sum_{k=1}^M X_{ijk}^o, \quad (5)$$

$$\sigma_{ij}^{o2} = \frac{1}{M-1} \sum_{k=1}^M (X_{ijk}^o - \langle X^o \rangle_{ij})^2, \quad (6)$$

where i , j , k , and O represent year from 1 to N ($=10$), pentad from 1 to 73, ensemble from 1 to M ($=10$), and observed SSTs, respectively. The results of these calculations are shown in Fig. 5. Roughly speaking, the overall features of the TISV indices from the observed SST simulations are very similar to the natural variability of the TISV depicted in Fig. 4. However, closer examination of the four plots shows that there is some year-to-year variability in the mean levels of TISV activity, although for the most part the size of the variations appears to be quite modest. One case worth highlighting is the January–March value of the summer mode precipitation index that shows a relatively low value for 1983. In addition to the year-to-year differences in ensemble-mean activity, there are also some differences in the standard deviations, that is, in the consistency of the 10 members of the ensemble to produce similar TISV activity levels. For example, the ensemble spread appears to be somewhat diminished during that same January–March 1983 period for the summer mode precipitation index. A similar decrease is seen

in the June–August 1989 for the winter mode precipitation index. These reductions in the ensemble spread, which are an indication of enhanced predictability, will be discussed in more detail below.

A quantitative measure of the size of the year-to-year variations in the mean TISV activity in the observed SST simulations is computed as follows:

$$[X^o]_j = \frac{1}{MN} \sum_{i=1}^N \sum_{k=1}^M X_{ijk}^o, \quad (7)$$

$$\sigma_j^{E2} = \frac{1}{N-1} \sum_{i=1}^N (\langle X^o \rangle_{ij} - [X^o]_j)^2, \quad (8)$$

where i , j , k , and O are the same as described above, and E denotes an estimate of the externally forced variability. Figure 6 shows the climatological average values of the ensemble-mean activity levels (thick solid lines; $[X^o]_j$) from the 10 different years shown in Fig. 5, along with the associated standard deviations (shaded area; σ_j^{E2}). The standard deviations indicate the size of the typical interannual variation in the ensemble-mean TISV activity for any given year from the observed SST simulations. Note that the size of these variations is only about 10% of the mean signal. More importantly, their size is only about 20% or less the size of the internal variability (e.g., Figs. 4), indicating that there is very

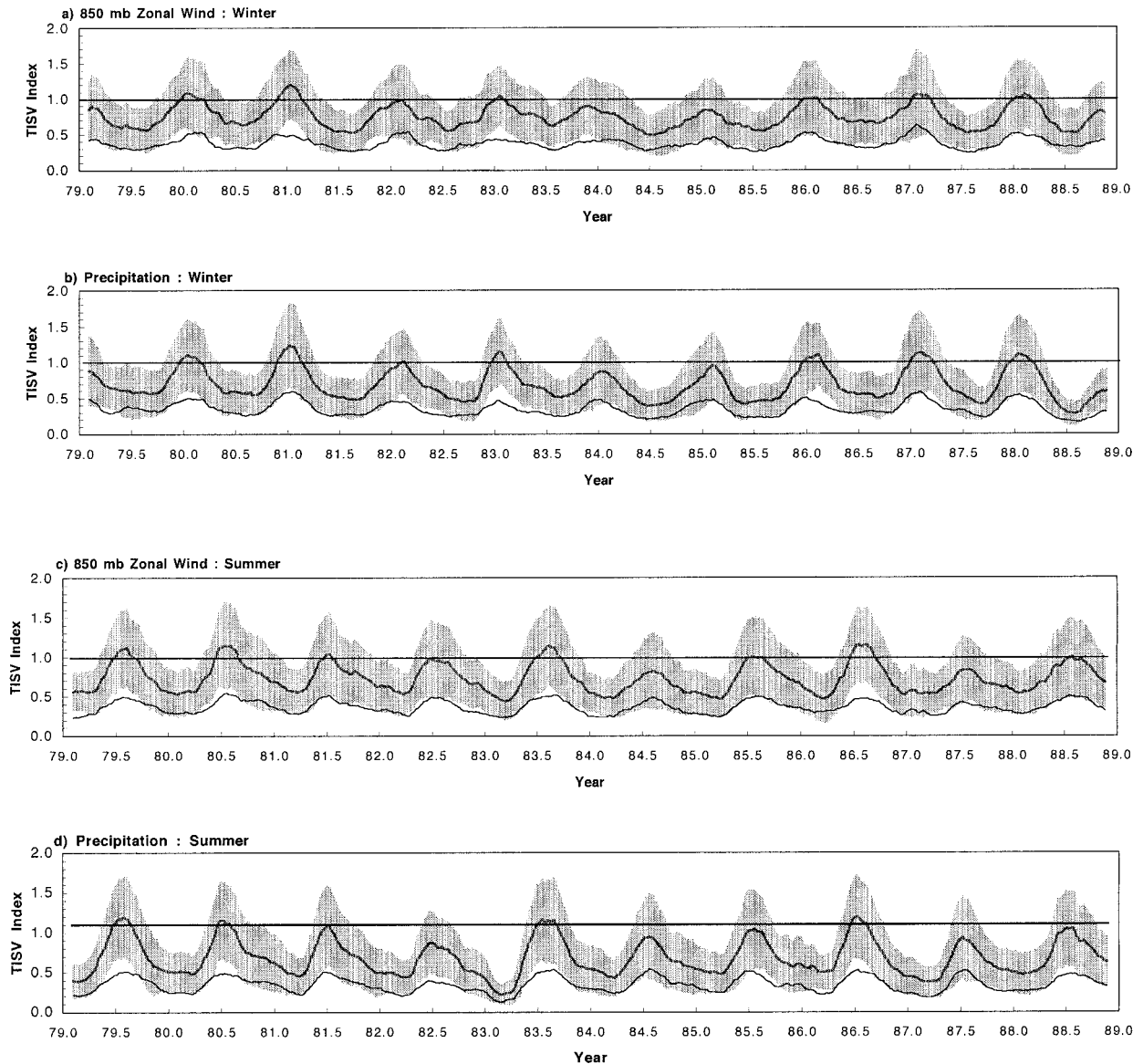


FIG. 5. Ensemble-mean (thick solid line; $\langle X^0 \rangle_{ij}$) and standard deviation (solid line and shading; σ_{ij}^0) of the TISV activity index from the ten 10-yr observed SST simulations for (a) U850 winter, (b) precipitation winter, (c) U850 summer, and (d) precipitation summer TISV modes. Curves have been smoothed using a 15-pentad running mean filter.

little externally forced interannual variability. The plots in Fig. 6 also show the mean TISV activity levels from the climatological SST simulation (thin dotted lines; i.e., thick solid lines from Fig. 4). Comparing the thin and thick solid lines shows that the general characteristics of the seasonal evolutions of the mean TISV activity are quite similar between the 10-yr climate simulation and the ten 10-yr simulations using observed SSTs. In fact, during most of the calendar year, the mean activity associated with the climatological SST simulation lies well within one standard deviation of the (10-yr) means associated with the ensemble simulations. However,

there are a few exceptions and these are likely due to the small differences between the climatological SSTs and the climatology of the observed SSTs and due to the fact that the comparisons are based on 10-yr (i.e., $N = 10$) averages of quantities with considerable (natural) variability.

Along with comparing the mean activity levels between the climate simulation and the observed SST simulations, it is also of interest to compare a measure of the reproducibility between these two. This can be done by computing the average values of the standard deviations over the 10 different simulation years shown

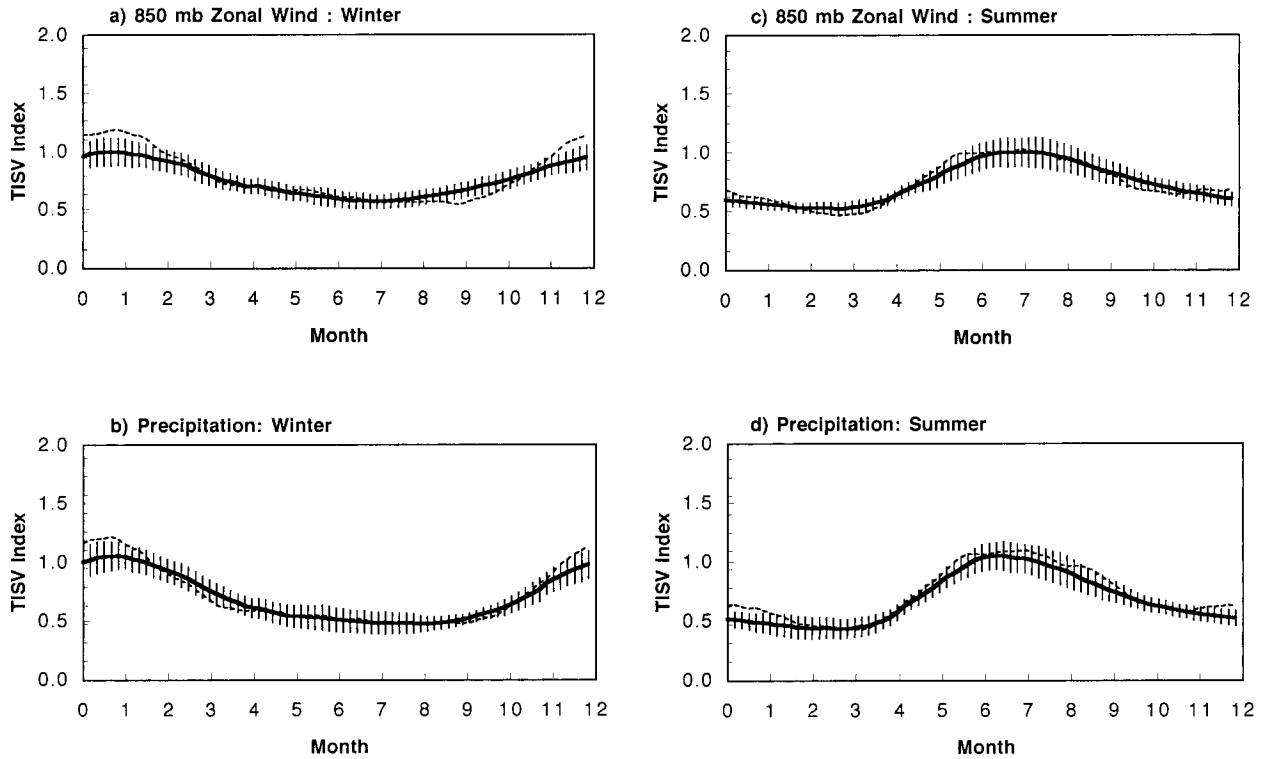


FIG. 6. Climatological mean (thick solid; $[X^O]_j$) and standard deviation (shading; σ_j^E) of ensemble-mean TISV activity indices from the ten 10-yr observed SST simulations for the (a) U850 winter, (b) precipitation winter, (c) U850 summer, and (d) precipitation summer TISV modes (i.e., averages and standard deviations of the thin dotted curves in Fig. 5). Thin dotted lines are the climatological mean TISV activity indices from the climatological SST simulation ($\langle X^C \rangle_j$); reproduced from the thick solid lines in Fig. 4).

in Fig. 5 (i.e., the thin solid lines) as well as the associated standard deviations of these averages:

$$[\sigma^{O2}]_j = \frac{1}{N} \sum_{i=1}^N \sigma_{ij}^{O2}, \quad (9)$$

$$\sigma_j^{Y2} = \frac{1}{N-1} \sum_{i=1}^N (\sigma_{ij}^{O2} - [\sigma^{O2}]_j)^2, \quad (10)$$

where i , j , and O are the same as described above, and V denotes a variance of variances. The mean values ($[\sigma^{O2}]_j$; not shown) depict the average intraensemble variation of the TISV activity across all 10 yr. A comparison of these values to σ_j^{C2} ; indicates that the typical year-to-year variations within the 10-yr climatological SST simulation is about the same as the intraensemble variations found in the observed SST simulation, averaged over all 10 yr (i.e., $[\sigma^{O2}]_j$). This implies that the typical variation in TISV activity across a set of simulations (10 in this case) forced by the same SST will be about the same whether it is a climatological or anomalous SST condition. In addition, the relatively small values of σ_j^{Y2} (~ 0.05) indicate that on average the ensemble for any given year has about the same statistical spread.

The comparisons described above between the climatological and observed SST simulations qualitatively indicate that the TISV activity levels are not that sen-

sitive to the imposed interannual SST anomalies. This can be further quantified by first computing an unbiased estimate of the externally forced TISV variability due to interannual SST anomalies, and then comparing this to the size of the internal variability of TISV. In the case of the former, one has to correct for the influence of the internal variability on σ^{E2} (e.g., Rowell et al. 1995). An estimate of this correction can be computed from

$$\sigma_j^{\text{SST}2} = \sigma_j^{E2} - \frac{1}{M} \sigma_j^{C2}. \quad (11)$$

Given the relatively small (large) values of σ_j^E (σ_j^C), this quantity typically ends up being small and even negative in some cases. This indicates that there is very little or no externally forced variability in this model ensemble. Fig. 7 shows the ratios:

$$\sigma_j^{\text{SST}} / \sigma_j^C \quad (12)$$

(i.e., the ratio between the externally forced and internal variability) for the periods of the year where $\sigma_j^{\text{SST}2}$ is positive (thick solid lines). Thus these graphs provide a seasonally dependent measure of the interannual predictability of the model's TISV. While the plots do suggest some seasonal dependence of TISV predictability, overall they indicate that the model calculations have

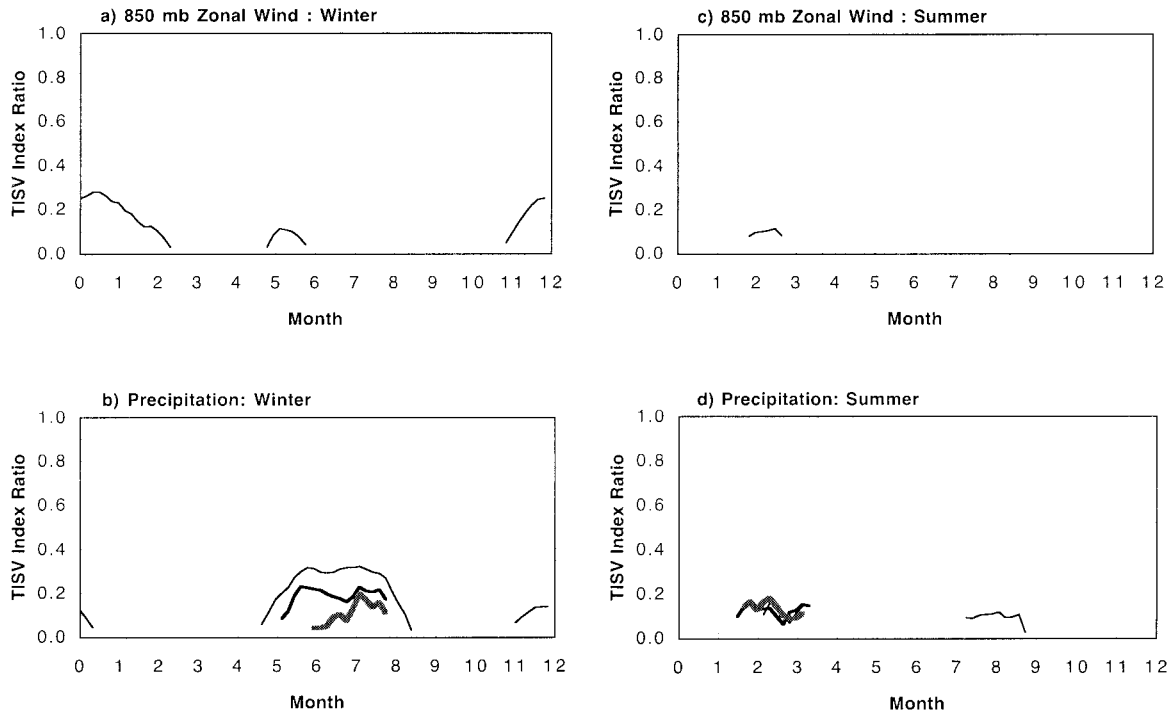


FIG. 7. Thick solid lines are the ratio between an estimate of the externally forced TISV variability due to interannual SST anomalies and the internal variability associated with TISV where each is represented by their standard deviation (i.e., σ^{SST}/σ^C) for the (a) U850 winter, (b) precipitation winter, (c) U850 summer, and (d) precipitation summer TISV modes. Thick gray lines are the same except when the analysis is performed by setting L equal to 9 instead of 2 in Eq. (2). Thin solid lines are the same except when the analysis is performed with an intraseasonal bandpass window of 35–70 days instead of 20–100 days.

little to no useful predictability associated with interannual variations in TISV as they might relate to interannual variations in SST. Put another way, this indicates that the anomalous variations in the ensemble-mean TISV activity values (Fig. 5) are largely driven by internal variations. The thick gray lines in Fig. 7 show the same results but for setting the number of modes retained in Eqs. (2)–(9) and the thin solid line shows the same results but for an intraseasonal bandpass window of 35–70 days. Retaining additional EOF modes in the analysis appears to have very little impact on the results. However, there is some indication that the narrower intraseasonal window increases the predictability slightly, particularly during the winter season for the winter mode(s), although the net result is still very little predictability.

Given the above lack of sensitivity to SST, it is not surprising that the anomalies in the ensemble mean TISV activity (i.e., $X_{ij}^o - \langle X^o \rangle_{ij}$) show little correlation with anomalous SST (not shown). Positive (negative) correlations exist between winter (summer) TISV precipitation activity and SST in the central and eastern Pacific; however, the magnitudes are about 0.5 or less, which for 10 degrees of freedom (i.e. 10 yr) is not significant. For the most part, the spatial structure of the correlations with SST for the U850-based activity are the same, just a bit weaker, with the main exception

being a relatively strong region of negative correlation in the tropical South Atlantic. Although again, the magnitude is only about 0.4. Thus, consistent with the above analysis, anomalous SST appears to have little influence on the interannual fluctuations of the overall intensity of the modeled MJO. This aspect of the study will be discussed further in section 5.

b. Interannual variations in TISV predictability

The analysis in the previous section indicates that, on average, the model calculations show very little interannual predictability of TISV. This was based on an assessment of all 10 model-simulated years together. However, it is still possible that specific modes during specific periods may be more or less predictable than others. This would imply that under certain circumstances the SST anomalies move the climate system to a more or less predictable state (e.g., Anderson et al. 1999; Palmer 1993; Barnston et al. 1994; Webster et al. 1998; Sperber et al. 2000). This is an important consideration, one that cannot be addressed with observations alone. As discussed in the introduction, some evidence for this is found in the predictability study by Slingo et al. (1999), although no direct analysis was performed in their study to determine if this was the case. In order to address this question, a temporal mea-

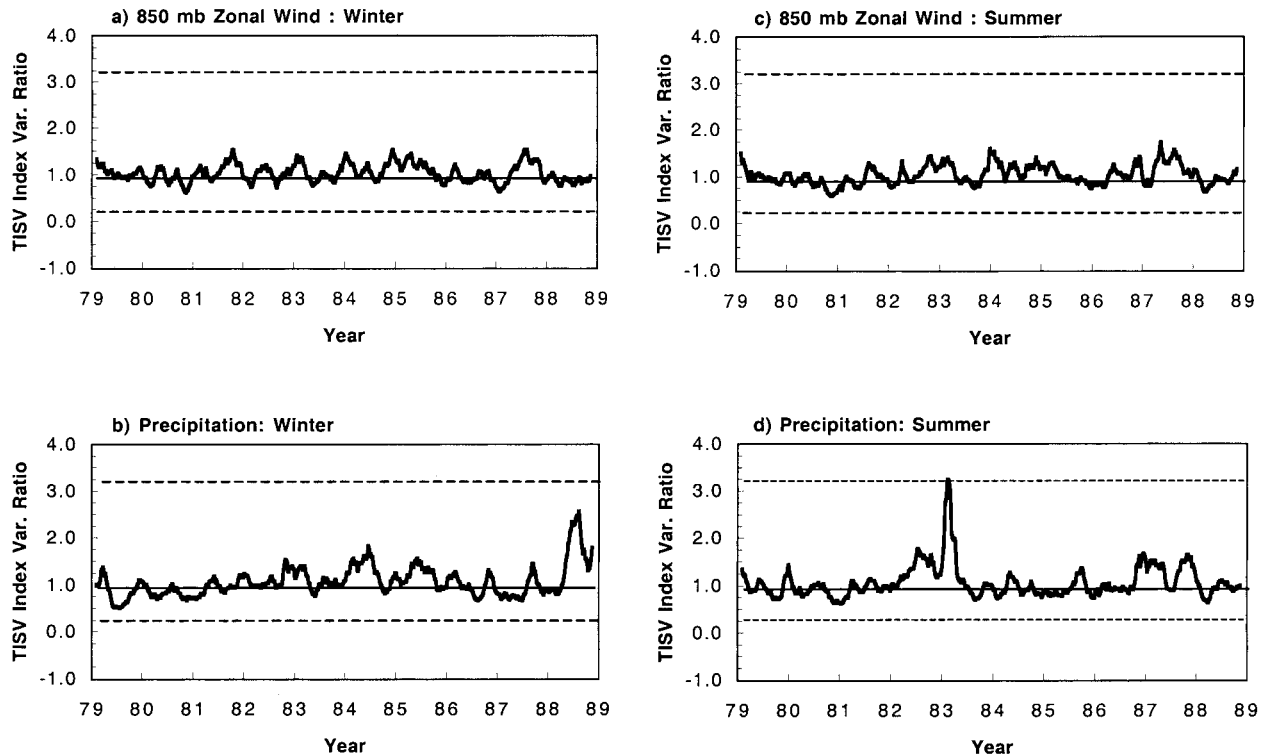


FIG. 8. Ratio between the average intraensemble variability (i.e., $[\sigma^2]_j$) from the observed SST simulations and the year-to-year intraensemble variability from the observed SST simulations (σ_{ij}^2 ; thin solid lines in Fig. 5). Dotted horizontal lines give 95% confidence intervals that the two population variances are different based on an F test with $N = 10$ for each sample size (Kanji 1993).

sure of the intraensemble reproducibility is needed. Such a measure can be constructed by taking the ratio between the 10-yr average of the intraensemble variability (i.e., $[\sigma^2]_j$) and the year-to-year intraensemble variability from the observed SST simulations (σ_{ij}^2 ; thin solid lines in Fig. 5). The former provides a measure of natural variability within the model (e.g., Fig. 6) while the latter provides a measure of how the external SST forcing modifies this natural variability. For example, if this ratio is larger than one, then the typical intraensemble variations in the externally forced simulations are smaller than the natural variability and thus there is a greater tendency for predictability than indicated, for example, in Fig. 7. The opposite implication would hold for a ratio smaller than one.

Figure 8 shows these variance ratios for the winter mode (Figs. 8a and 8c) and summer mode (Figs. 8b and 8d) TISV activity indices, along with an indication of the 95% confidence level (horizontal bars). Most evident is the period of enhanced summer mode reproducibility during late 1982 and early 1983 for the precipitation index. This can be seen qualitatively in Fig. 5d, when an especially low intraensemble standard deviation occurred during this period and the 10 members of the ensemble seem to agree especially well. The magnitude of the summer mode ratio during this particular period suggest that the intraensemble variability reduces to about one-third of the size of the natural variability ac-

ording to the precipitation ratio, and thus would suggest a more predictable scenario. Another period of marked change in reproducibility occurs during 1988 for the winter mode precipitation ratio, although this excursion is not statistically significant at the 95% confidence level.

The result discussed above suggests that there may be some enhanced predictability of the summer mode TISV activity level associated with precipitation during the strong El Niño of 1982/83. On the other hand, this enhancement was not observed in the U850 summer mode TISV activity index for the same period, and there was only a modest enhancement in the same reproducibility measure during the El Niño of 1986/87. Thus even though there is an indication of statistical significance for this finding, there is still reason to have some suspicion about its robustness. As an additional test of robustness, a similar calculation of reproducibility can be done for the CLIVAR ensemble of 2-yr simulations since this period also encompassed an El Niño similar in strength to the 1982/83 case. Figure 9 shows precipitation-based TISV activity index information for the summer and winter modes from this ensemble of 2-yr simulations. The top two panels are analogous to the information plotted in Fig. 5 while the bottom two panels are analogous to Fig. 8. Note that in this case, the measure of internal variability used for the construction of the variance ratios comes from the 10-yr simulations

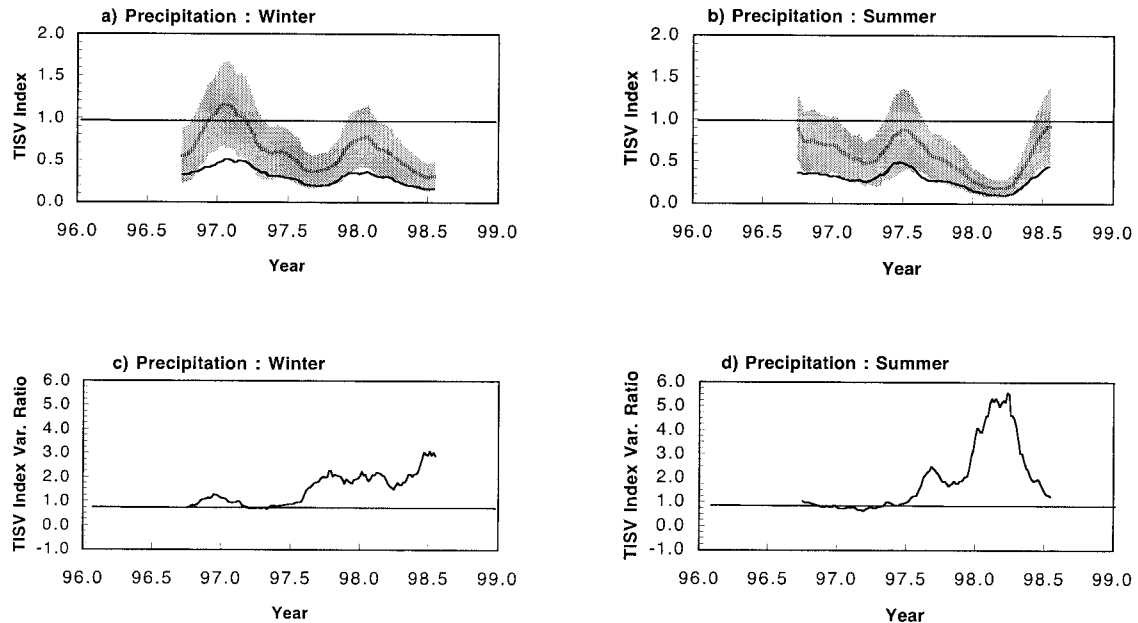


FIG. 9. (a) and (b) Same as Fig. 5 except for the ensemble of 2-yr simulations (see section 2). (c) and (d) Same as Fig. 8 except for the ensemble of 2-yr simulations. In both cases, only TISV activity associated with precipitation is given.

described above. Evident is the same sort of enhanced signature of reproducibility for the summer TISV mode during the winter period associated the strong 1997/98 El Niño. In addition to this similarity, both episodes exhibit anomalously low ensemble-mean TISV activity for the summer mode (not shown). An examination of the significance of these anomalies indicates that both are significant at the 95% level. This is based on the assumption that the ensemble-mean climatology from the 10-yr simulations (i.e., Fig. 6) adequately describes the climatology for both the 10- and 2-yr simulations, and thus it is used in both cases to determine the ensemble-mean anomaly. Given the differences in the experimental design of these two experiments (see section 2), there is some uncertainty introduced here regarding the specific values of the variance ratios and the anomalies. In any case, this uncertainty is not large enough to alter the qualitative aspects of the above discussion.

c. Generalized intraseasonal predictability

Up to this point, the discussion has entirely focused on predictability of organized modes of TISV. The findings thus far are that very little useful predictability of these modes is evident from the sets of model simulations analyzed here, apart from some indication that the summer TISV mode may exhibit a reproducible reduction in activity during winter periods that are associated with very strong El Niños. To further explore the predictability of TISV, the constraint of organized modes will now be relaxed to determine what, if any, sorts of generalized TISV predictability might exist. The computation of predictability closely follows the framework

described in section 4a, except for the following. Rather than have one index for the entire global Tropics for a given field and mode [e.g., winter mode precipitation TISV index via Eq. (2)], an index for TISV activity is constructed for every grid point (cf. Yang et al. 1998). This index is computed by simply taking the running standard deviation of the bandpassed model output at each grid point, where the box length is 20 pentads. If this index is represented as X_{ijk}^o , then the discussion associated with Eqs. (5)–(10) applies with the understanding that X_{ijk}^o has a spatial dependence. A seasonally dependent predictability ratio, made up in this case of 73 pentads, can then be constructed for each grid point using Eq. (12). In this case, the internal variability is estimated from Eq. (9), and thus $[\sigma^o]_j$ replaces σ_j^c in Eqs. (11) and (12).

Figure 10a shows the annual average of these predictability ratios for the case where precipitation is used to represent TISV. This diagram shows that the intraseasonal variability in precipitation from this model ensemble is only predictable over the equatorial central Pacific Ocean. Correlations computed between ensemble-mean TISV values at each grid point (i.e., $\langle X^o \rangle_{ij}$) and SST from the equatorial central Pacific (not shown) show that the increase in TISV over the central Pacific is associated with SST warming ($r \sim 0.7$). Thus, the predictability of generalized TISV in this case is strongly determined by the large-scale local warming and cooling associated with ENSO. Figures 10b–d illustrate the same result but for the cases when the data are filtered via EOF decomposition prior to computing the TISV activity index values. In the cases of Figs. 10b–d, the analysis retained 20, 9, and 2 modes, respectively.

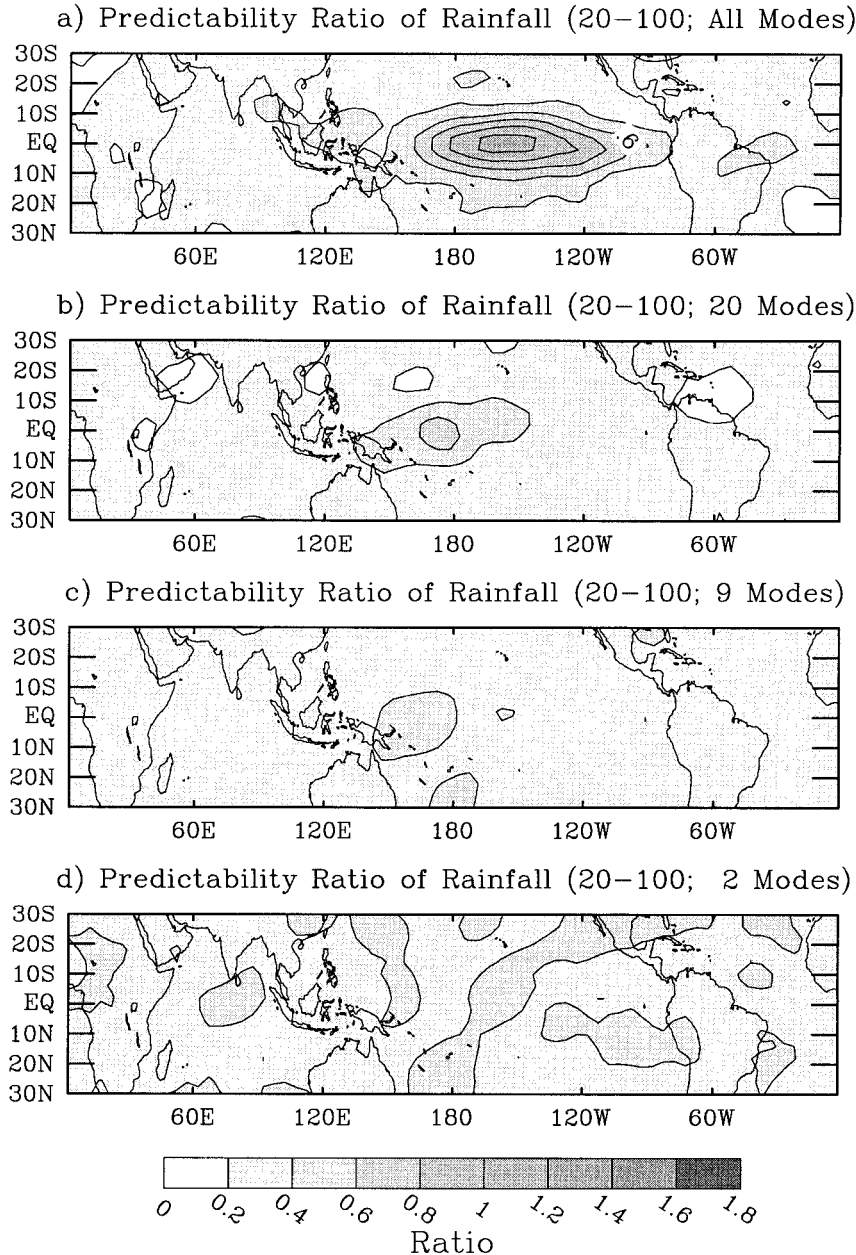


FIG. 10. Annual average predictability ratios for generalized TISV based on precipitation. In this case, predictability is based on a TISV index computed at each model grid point by taking the running standard deviation of the bandpassed model output, where the box length is 20 pentads (see section 4c for details). (a) No additional filtering of the bandpassed data prior to computing the TISV index at each point. (b) Prior to computing the TISV index, the bandpassed data were filtered by retaining only the first 20 EOF modes. (c) Same as (b) except for retaining only 9 modes. Same as (b) except for retaining only 2 modes.

This EOF filtering acts to retain spatially coherent intraseasonal features. The greatly reduced predictability values associated with these EOF-filtered cases indicate that on average nearly all of the predictable variance associated with Fig. 10a is incoherent with intraseasonal variations away from the western/central Pacific. Thus, most of the predictable variations exhibited in that figure

are attributable to “random” intraseasonal fluctuations in the “stationary” heating anomalies associated with El Niño, which in some cases may in turn be brought about by intraseasonal variations in the large-scale SST anomaly. It is also possible that part of this predictable variance is resulting from the individual MJO events propagating farther east during an El Niño event. How-

ever, since the retention of a limited number of EOF modes would not be able to capture this feature, one would not expect to find it strongly exhibited in the mean predictability ratios for the three EOF-filtered cases, although there is some hint of it in Fig. 10b.

5. Summary and discussion

The objective of this study is to examine the relationship between interannual SST variability and the activity and predictability of tropical intraseasonal variability (TISV). The NASA GLA general circulation model, coupled to a weakly interacting slab ocean mixed layer, was chosen for this study due to its relatively realistic representation of TISV (Slingo et al. 1996; Waliser et al. 1999b). One 10-yr simulation forced by climatological SST was conducted for the purposes of evaluating the natural variability associated with TISV, that which is independent of any anomalous SST forcing. Ten-member ensemble simulations forced by observed SSTs were used to assess the externally forced variability associated with large-scale anomalous SST. TISV was identified and analyzed using precipitation and 850-hPa zonal wind (U850). These data were bandpassed with a 20–100-day bandpass filter to isolate TISV. The filtered data were then separated in “winter” and “summer” to better isolate the dominant TISV modes of variability, which includes eastward equatorial propagating mode that is prevalent in Northern Hemisphere winter (winter mode) and the northeastward propagating mode that is prevalent in northern summer (summer mode). The basic structure of these two modes was captured using EOF decomposition analysis. TISV activity indices were computed from the combined variance of the amplitude time series of the leading two EOFs.

The TISV activity indices from the climatological SST simulation exhibited considerable natural variability in both the winter and summer TISV modes, with the year-to-year fluctuations being about half the size of the mean levels of MJO activity. In comparison, the variability of the ensemble mean TISV activity indices from the observed SST simulations was quite small. Using the above estimations of internally generated and externally forced MJO variability, a measure of predictability was constructed for the interannual fluctuations in MJO variability that are related to interannual SST anomalies [Eq. (12)]. While this measure exhibited some weak seasonal dependence, on average it indicated that virtually none of the ensemble-mean TISV variance for either the summer or winter MJO mode could be ascribed to external forcing. Sensitivity tests showed that this result was only modestly affected by the choice of the bandpass window or the number of modes retained for the construction of the TISV indices.

The above results regarding overall predictability are qualitatively similar to those of Slingo et al. (1999) and Gualdi et al. (1999), who found that only about 10%

and 20%, respectively, of the MJO winter mode activity variance of their ensembles could be ascribed to external forcing. The interest here was to examine the same sort of question: 1) using a different model that also exhibits fairly realistic TISV, 2) using a more realistic SST boundary condition (i.e., coupled slab mixed layer), 3) considering the northeastward-propagating (summer) mode in addition to the eastward-equatorial-propagating (winter) mode, and 4) including an investigation of the seasonal and interannual dependence of TISV predictability. The even lower predictability values for the present study could be due to a number of factors. First, it may be that the form of the GLA model used in this study may simply have more internal variability associated with the MJO than the other two models. This could be due to the model's MJO representation and associated model physics and/or due to the inclusion of the interactive ocean mixed layer, which provides intraseasonal SST anomalies that evolve differently for each member of the ensemble (see additional discussion below). If the influence from SST coupling on the MJO found for the GLA model (Waliser et al. 1999b) could be presumed to extend to the UKMO and ECHAM4 models, then it is likely that SST coupling may play some role since this coupling was found to increase the model's MJO variability for the same low-frequency SST conditions. If this is the case, and the coupling influence can be considered a realistic one, then those studies that are based on specified SSTs may be overestimating the amount of MJO predictability. Second, it may be that the MJO in the GLA model is simply less sensitive to anomalous SST. Finally, it is possible that the ensemble characteristics (i.e., number and time period) may be affecting the results. For example, higher value associated with the Gualdi et al. study over the Slingo et al. study appeared to stem primarily from their larger ensemble size. However, even when only 4 of the 15 members were analyzed from the ECHAM4 ensemble, it still showed high predictability values (~10%) than those exhibited here. In regards to the period analyzed, it is worth mentioning that a large fraction of the externally forced variability in the Gualdi et al. study occurred during the 9-yr overlapping period used in this study (i.e., 1980–88). Thus it is not obvious that ensemble characteristics played a significant role in the differences between predictability values found in these three studies.

Given the weak influence that SST anomalies have on the model ensemble, it is not surprising that the anomalous ensemble-mean TISV activity is only weakly correlated to interannual SST anomalies. Typically, the correlations with eastern Pacific SST anomalies is about 0.5 at most, which is insignificant for the size of the record analyzed. It should be pointed out that this in itself is not inconsistent with observational analyses, which also show correlation relationships that are either not significant or only marginally so (e.g., Fink and Speth 1997; Hendon et al. 1999; Slingo et al. 1999).

This is even the case when the observed TISV indices are constructed based on this study's formulation [i.e., Eq. (2); also see discussion below] and correlated with SST over the 1979–88 period employed in this study (not shown). The aspect which is a bit at odds with the observations is that the weak correlation that does exist with eastern Pacific SST is positive in the present study (similarly for Slingo et al. 1999) while it is weakly negative in the observed studies. However, if the strong El Niños of 1982/83 and 1997/98 are removed from the observed record, the observed tendency weakens and reverses sign (Hendon et al. 1999). Given the tenuous relationship between anomalous SST and TISV activity, it is not clear if this difference in correlation tendency between the model(s) and observations is due to a shortcoming of the models or insufficient sampling in the observations given what appears to be a highly chaotic process.

Analysis was also performed to determine if and how the intraensemble reproducibility was influenced by interannual variations in SST. To do so, the ratio between a measure of natural variability for a given TISV index and the intraensemble variability was computed (Fig. 9). In cases where the intraensemble variability was less (more) than the natural variability, this implies the anomalous SST was constraining the TISV to be more (less) reproducible within the ensemble than the case with no anomaly. The main finding from this portion of the study was that while the model ensembles indicate that there is little or no overall predictability, the El Niños of 1982/83 and 1997/98 produced a significant enhancement in the intraensemble reproducibility for the summer TISV mode. Thus very strong El Niños may have some influence over the amount of internal variability associated with the summer TISV mode and even its overall level of activity (see discussion below).

Finally, to determine what if any sorts of TISV activity might be predictable on interannual timescales, a generalized TISV index and associated predictability measure were computed at each model grid point based on the amount of time-averaged (~ 100 days) bandpassed variance. These predictability values showed some evidence that intraseasonal variance with no constraints on spatial structure is predictable over the central and eastern equatorial Pacific in association with ENSO-related SST anomalies. However, when the data are filtered via EOFs to only retain TISV that has some spatial structure, the predictability values diminish rapidly. This aspect of the analysis also showed some indication that the model exhibits some capability at reproducing the zonal shifts in the eastern edge of the MJO convective "envelope" in association with ENSO-driven SST variations.

As mentioned above, these model simulations were undertaken with what is believed to be a more realistic boundary condition than simply specifying a fixed SST. Namely, a weak SST feedback has been included by coupling a slab mixed layer model that is designed to

provide high-frequency ($< \sim 100$ days) SST anomalies, which interact with the model TISV. In a previous study using climatological SSTs (Waliser et al. 1999b), this coupling scheme was shown to improve the simulation characteristics of the MJO (i.e., winter mode TISV). As discussed in section 2, this coupling scheme can produce some relatively longer-lived SST anomalies due to the fact that the ensemble simulations use observed SSTs yet the flux anomaly used in the formulation of the SST anomaly model is computed using a 12-month flux climatology. On the one hand, it is highly desirable to have the SST coupling as it is expected to be more realistic and may even be a better approximation to future operational conditions associated with interannual climate predictions. On the other hand, it makes it more difficult to separate natural variability from that associated with anomalous SST forcing, since the latter is slightly different for each simulation due to the weak SST coupling. Examination of the SST from the 10 members of the ensemble shows that the intraensemble variations in SST are rather modest compared to the interannual variability that necessarily needs to be imposed for each simulation. Figure 11 shows the mean anomalous SST from the 10 observed SST simulations from the equatorial eastern Pacific and central Indian Oceans. In each case, the annual cycle based on the observed (fixed) SST has been removed. The dark shaded area represents the mean SST anomalies from the 10 simulations plus and minus the standard deviation associated with this mean. The thin solid line is the observed SST anomaly. From these two plots, it is evident that the interannual character of the SST is largely the same for all 10 experiments, especially so for the interannual variations occurring in the eastern Pacific in association with ENSO. This suggests that the additional SST variability produced by the weak coupling to the ocean mixed layer is not likely to be so large as to change the basic interannual character of the SST for each member of the ensemble.

Finally, it is worth examining how the model's ensemble simulation of interannual TISV activity compares to observations. Figure 12 shows the model activity indices for both the winter and summer TISV modes for precipitation. The gray solid line is the 10-member ensemble mean, the shading is the associated standard deviation. This part of the plot is the same as that shown in Figs. 5b,d. The thin solid lines are the maximum and minimum TISV index values from the ten 10-yr simulations. The thick solid lines are the corresponding TISV activity indices computed from observations. The data used for these are the Xie and Arkin (1997) pentad values of multiinstrument merged precipitation estimates. The observed TISV activity indices were computed in the same manner as from the model-derived indices (see section 3). The observed EOF patterns used in the construction (not shown) show a significant degree of similarity with the model patterns (i.e., Figs. 1 and 2); however, they display slightly more var-

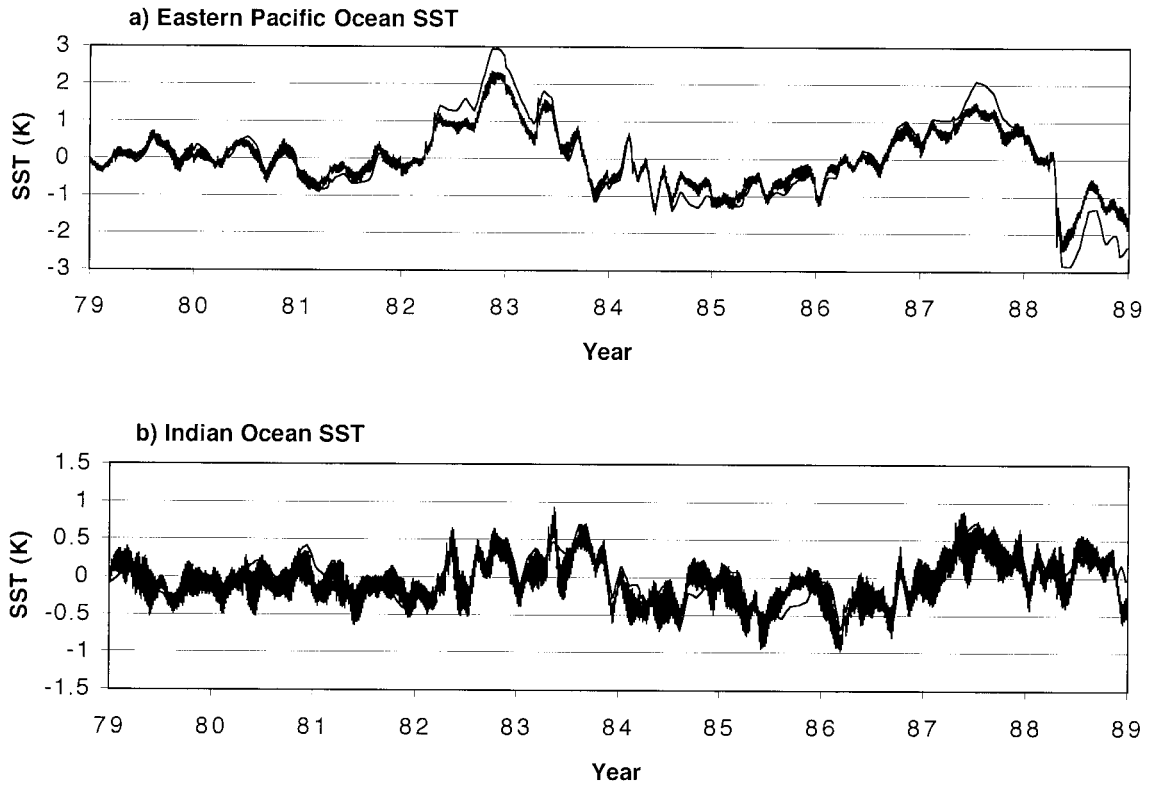


FIG. 11. Equatorial (a) eastern Pacific Ocean (2°S, 120°W) and (b) Indian Ocean (2°S, 85°E) SST anomalies from the 10 ensemble simulations. Dark shading represents the ensemble-mean value plus and minus the standard deviation. Thin solid line is the actual observed SST anomalies. In the cases of the SST from the simulations, the anomalies were computed by using the observed climatology.

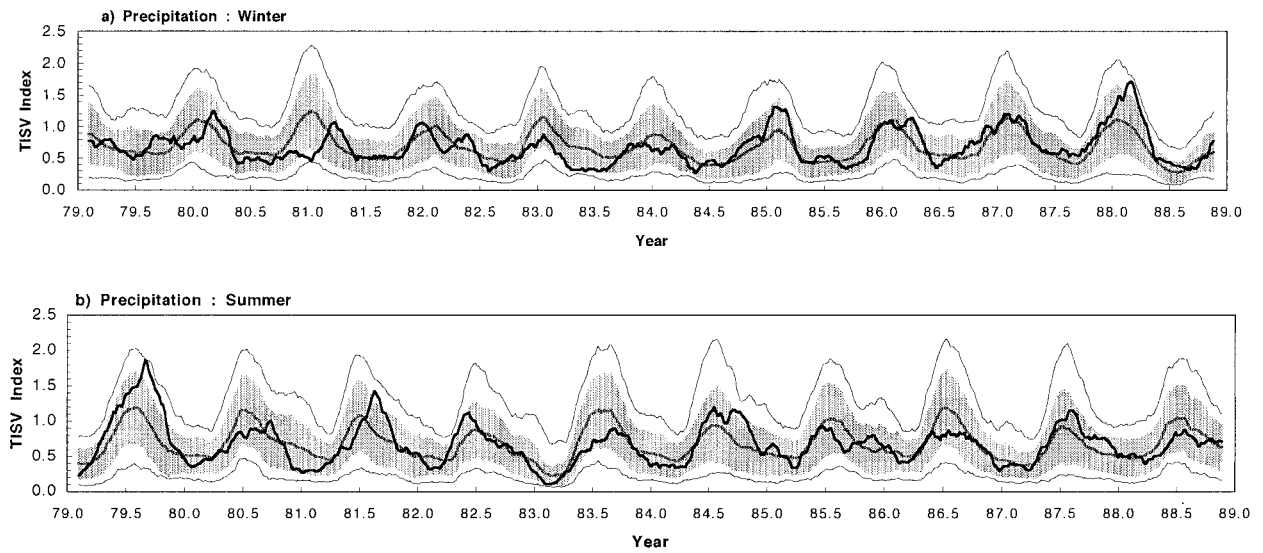


FIG. 12. Ensemble-mean (light dashed line) and standard deviation (shading) of the TISV activity index from the ten 10-yr observed SST simulations for (a) precipitation winter and (d) precipitation summer TISV modes. Thin solid curves are the maximum and minimum TISV index values from the 10 simulations. Thick solid curve is the TISV activity index computed from observations (see section 5 for details). Curves have been smoothed using a 15-pentad running mean filter.

iability in the Indian Ocean region. The plots in Fig. 12 show that the TISV variability associated with the “single manifestation” from observations always lies within the maximum and minimum values from the 10-member ensemble and almost always lies within one standard deviation. This implies that, at least statistically speaking, any one of the ensemble members might be representative of the evolution of TISV activity found in the observations. Similar results were found to hold for the ten 2-yr simulations. Thus, other than the modest differences in the spatial variability of the dominant TISV modes (e.g., Figs. 1 and 2), this ensemble of simulations could be said to reasonably capture the observed variations in TISV activity during the two simulated periods. As an indication that some promise may exist in the area of interannual predictability of intraseasonal variability, both the observations and the ensemble-mean TISV activity indices exhibit a fairly substantial decrease in summer mode TISV activity during the winter periods of 1982/83 and 1997/98. These are the same periods when the reproducibility between the ensemble members was significantly enhanced. Thus, on rare occasions, there may be instances where ensemble prediction of extremes in TISV activity may display some success.

Acknowledgments. Support for this study was provided by the Climate Dynamics Program in the Atmospheric Sciences Division of the National Science Foundation under Grant ATM-9712483 (DW and ZZ) and by Dr. K. Bergman of the NASA Mission to Planet Earth Office (WL and JK). The origin of this study stems from the second authors masters thesis at the State University of New York at Stony Brook. In this regard, the first two authors would like to thank professors Sultan Hameed and Minghua Zhang for their comments and suggestions regarding this work. We would also like to thank Harry Hendon, Roland Madden, and an additional anonymous reviewer for their helpful comments and suggestions, and In-Sik Kang for his effort in coordinating the WCRP-CLIVAR Asian-Australian Monsoon Atmospheric GCM Intercomparison Project. Acknowledgment is made to NCAR, which is sponsored by the National Science Foundation, for the computing time used in this research. This study’s analysis and presentation benefited from the use of the NCAR Graphics Package and Seaspace Corporation’s TeraScan software system.

REFERENCES

- Anderson, J., H. van den Dool, A. Barnston, W. Chen, W. Stern, and J. Ploshay, 1999: Present-day capabilities of numerical and statistical models for atmospheric extratropical seasonal simulation and prediction. *Bull. Amer. Meteor. Soc.*, **80**, 1349–1362.
- Arakawa, A., and W. H. Schubert, 1974: Interaction of a cumulus cloud ensemble with the large scale environment, Part I. *J. Atmos. Sci.*, **31**, 674–701.
- , and V. R. Lamb, 1977: Computational design of the basic dynamical processes of the UCLA general circulation model. *Methods in Computational Physics*, J. Chang, Ed., Academic Press, 173–265.
- Barnston, A. G., and Coauthors, 1994: Long-lead seasonal forecasts—Where do we stand? *Bull. Amer. Meteor. Soc.*, **75**, 2097–2114.
- Duchon, C. E., 1979: Lanczos filter in one and two dimensions. *J. Appl. Meteor.*, **18**, 1016–1022.
- Ferranti, L., T. N. Palmer, F. Molteni, and K. Klinker, 1990: Tropical-extratropical interaction associated with the 30–60 day oscillation and its impact on medium and extended range prediction. *J. Atmos. Sci.*, **47**, 2177–2199.
- Fink, A., and P. Speth, 1997: Some potential forcing mechanisms of the year-to-year variability of the tropical convection and its intraseasonal (25–70 day) variability. *Int. J. Climatol.*, **17**, 1513–1534.
- Gates, W. L., and A. B. Nelson, 1975: A new (revised) tabulation of the Scripps topography on a one-degree global grid. Part 1: Terrain heights. The Rand Corporation Tech. Rep. R-1276-1-ARPA, 132 pp.
- Gualdi, S., A. Navarra, and G. Tinarelli, 1999: The interannual variability of the Madden-Julian oscillation in an ensemble of GCM simulations. *Climate Dyn.*, **15**, 643–658.
- Harshvardhan, R. Davies, D. A. Randall, and T. G. Corsetti, 1987: A fast radiation parameterization for general circulation models. *J. Geophys. Res.*, **92**, 1009–1026.
- Helfand, H. M., and J. C. Labraga, 1988: Design of a non-singular level 2.5 second order closure model for prediction of atmospheric turbulence. *J. Atmos. Sci.*, **45**, 113–132.
- Hendon, H. H., and B. Liebmann, 1990a: A composite study of onset of the Australian summer monsoon. *J. Atmos. Sci.*, **47**, 2227–2240.
- , and —, 1990b: The intraseasonal (30–50 day) oscillation of the Australian summer monsoon. *J. Atmos. Sci.*, **47**, 2909–2923.
- , and M. L. Salby, 1994: The life cycle of the Madden-Julian oscillation. *J. Atmos. Sci.*, **51**, 2225–2237.
- , C. Zhang, and J. D. Glick, 1999: Interannual variation of the Madden-Julian oscillation during austral summer. *J. Climate*, **12**, 2538–2550.
- , B. Liebmann, M. Newman, J. D. Glick, and J. Schemm, 2000: Medium-range forecast errors associated with active episodes of the Madden-Julian oscillation. *Mon. Wea. Rev.*, **128**, 69–86.
- Higgins, R. W., and K. C. Mo, 1997: Persistent North Pacific circulation anomalies and the tropical intraseasonal oscillation. *J. Climate*, **10**, 224–244.
- Jones, C., D. E. Waliser, J. K. Schemm, and W. K. Lau, 2000: Prediction skill of the Madden-Julian oscillation in dynamical extended range forecasts. *Climate Dyn.*, **16**, 273–289.
- Kalnay, E., R. Balgobind, W. Chao, D. Edelmann, J. Pfandtner, L. Takacs, and K. Takano, 1983: Documentation of the GLAS fourth order general circulation model. Vol. 1, NASA Goddard Space Flight Center Tech. Memo. 86064, 436 pp.
- Kanji, G. K., 1993: *100 Statistical Tests*. Sage Publications, 216 pp.
- Kessler, W. S., and R. Kleeman, 2000: Rectification of the Madden-Julian oscillation into the ENSO cycle. *J. Climate*, **13**, 3560–3575.
- , M. J. McPhaden, and K. M. Weickmann, 1995: Forcing of the intraseasonal Kelvin waves in the equatorial Pacific. *J. Geophys. Res.*, **100**, 10 613–10 631.
- Lau, K. M., and P. H. Chan, 1986: Aspects of the 40–50 day oscillation during the northern summer as inferred from outgoing longwave radiation. *Mon. Wea. Rev.*, **114**, 1354–1367.
- , and T. J. Phillips, 1986: Coherent fluctuations of extratropical geopotential height and tropical convection in intraseasonal time scales. *J. Atmos. Sci.*, **43**, 1164–1181.
- , and P. H. Chan, 1988: Intraseasonal and interannual variations of tropical convection: A possible link between the 40–50 day oscillation and ENSO? *J. Atmos. Sci.*, **45**, 506–521.
- Liebmann, B., and D. L. Hartmann, 1984: An observational study of tropical-midlatitude interaction on intraseasonal time scales during winter. *J. Atmos. Sci.*, **41**, 3333–3350.

- Lord, S. J., and A. Arakawa, 1980: Interaction of a cumulus cloud ensemble with the large-scale environment. Part II. *J. Atmos. Sci.*, **37**, 2677–2962.
- Madden, R. A., and P. R. Julian, 1971: Dection of a 40–50 day oscillation in the zonal wind in the tropical pacific. *J. Atmos. Sci.*, **28**, 702–708.
- , and —, 1972: Description of global-scale circulation cells in the Tropics with a 40–50 day period. *J. Atmos. Sci.*, **29**, 1109–1123.
- , and —, 1994: Observation of the 40–50-day tropical oscillation—A review. *Mon. Wea. Rev.*, **122**, 814–837.
- McPhaden, M. J., 1999: Climate oscillations—Genesis and evolution of the 1997–98 El Niño. *Science*, **283**, 950–954.
- Moore, A. M., and R. Kleeman, 1999: Stochastic forcing of ENSO by the intraseasonal oscillation. *J. Climate*, **12**, 1199–1220.
- Murakami, T., L. X. Chen, A. Xie, and M. L. Shrestha, 1986: Eastward propagation of 30–60 day perturbations as revealed from outgoing longwave radiation data. *J. Atmos. Sci.*, **43**, 961–971.
- Palmer, T. N., 1993: Extended-range atmospheric prediction and the Lorenz model. *Bull. Amer. Meteor. Soc.*, **74**, 49–66.
- Phillips, T. J., 1996: Documentation of the AMIP models on the World Wide Web. *Bull. Amer. Meteor. Soc.*, **77**, 1191–1196.
- Rowell, D. P., C. K. Folland, K. Maskell, and M. N. Ward, 1995: Variability of summer rainfall over tropical North Africa (1902–1992): Observations and modeling. *Quart. J. Roy. Meteor. Soc.*, **121**, 699–704.
- Salby, M. L., and H. H. Hendon, 1994: Intraseasonal behavior of clouds, temperature and motion in the Tropics. *J. Atmos. Sci.*, **51**, 2207–2224.
- , R. Garcia, and H. H. Hendon, 1994: Planetary circulation in the presence of climatological and wave-induced heating. *J. Atmos. Sci.*, **51**, 2344–2367.
- Sellers, P. J., Y. Mintz, Y. C. Sud, and A. Dalcher, 1986: A simple biosphere model (SiB) for use within general circulation models. *J. Atmos. Sci.*, **43**, 505–531.
- Shapiro, R., 1970: Smoothing, filtering and boundary effects. *Rev. Geophys. Space Phys.*, **8**, 359–387.
- Slingo, J. M., and R. A. Madden, 1991: Characteristics of the tropical intraseasonal oscillation in the NCAR community climate model. *Quart. J. Roy. Meteor. Soc.*, **117**, 1129–1169.
- , and Coauthors, 1996: Intraseasonal oscillations in 15 atmospheric general circulation models: Results from an AMIP diagnostic subproject. *Climate Dyn.*, **12**, 325–357.
- , D. P. Rowell, K. R. Sperber, and F. Nortley, 1999: On the predictability of the interannual behavior of the Madden–Julian oscillation and its relationship with El Niño. *Quart. J. Roy. Meteor. Soc.*, **125**, 583–610.
- Sperber, K. R., J. M. Slingo, P. M. Inness, and K.-M. Lau, 1996: On the maintenance and initiation of the intraseasonal oscillation in the NCEP/NCAR reanalysis and the GLA and UKMO AMIP simulations. *Climate Dyn.*, **13**, 769–795.
- , —, and H. Annamalai, 2000: Predictability and the relationship between subseasonal and interannual variability during the Asian summer monsoon. *Quart. J. Roy. Meteor. Soc.*, **126**, 2545–2574.
- Sud, Y. C., and G. K. Walker, 1992: A review of recent research on improvement of physical parameterizations in the GLA GCM. *Physical Processes in Atmospheric Models*, D. R. Sikka and S. S. Singh, Eds., Wiley Eastern Ltd., 422–479.
- Waliser, D. E., C. Jones, J. K. Schemm, and N. E. Graham, 1999a: A statistical extended-range tropical forecast model based on the slow evolution of the Madden–Julian oscillation. *J. Climate*, **12**, 1918–1939.
- , K. M. Lau, and J.-H. Kim, 1999b: The influence of coupled sea surface temperatures on the Madden–Julian oscillation: A model perturbation experiment. *J. Atmos. Sci.*, **56**, 333–358.
- Wang, B., and H. Rui, 1990a: Dynamics of the coupled moist Kelvin–Rossby wave on an equatorial beta plane. *J. Atmos. Sci.*, **47**, 397–413.
- , and —, 1990b: Synoptic climatology of the transient tropical intraseasonal convection anomalies. *Meteor. Atmos. Phys.*, **44**, 43–61.
- , and X. Xie, 1998: Coupled modes of the warm pool climate system. Part I: The role of air–sea interaction in Madden–Julian oscillation. *J. Climate*, **11**, 2116–2135.
- Webster, P. J., V. O. Magana, T. N. Palmer, J. Shukla, R. A. Tomas, M. Yanai, and T. Yasunari, 1998: Monsoons: Processes, predictability, and the prospects for prediction. *J. Geophys. Res.*, **103** (C7), 14 451–14 510.
- Wei, L., R. Yu, and L. Hailong, 2001: Responses of Madden–Julian oscillation in community climate model to different sea surface temperature forcing. *J. Ocean Univ. Qingdao*, in press.
- Weickmann, K. M., 1983: Intraseasonal circulation and outgoing radiation modes during Northern Hemisphere winter. *Mon. Wea. Rev.*, **111**, 1838–1858.
- , 1991: El Niño/Southern Oscillation and Madden–Julian (30–60 day) oscillations during 1981–1982. *J. Geophys. Res.*, **96**, 3187–3195.
- , G. R. Lussky, and J. E. Kutzbach, 1985: Intraseasonal (30–60 day) fluctuations of outgoing longwave radiation and 250 mb stream function during northern winter. *Mon. Wea. Rev.*, **113**, 941–961.
- Xie, P., and P. A. Arkin, 1997: Global precipitation: A 17-year monthly analysis based on gauge observations, satellite estimates, and numerical model outputs. *Bull. Amer. Meteor. Soc.*, **78**, 2539–2558.
- Xue, Y.-K., P. J. Sellers, J. L. Kinter II, and J. Shukla, 1991: A simplified biosphere model for global climate studies. *J. Climate*, **4**, 345–364.
- Yang, X.-Q., J. L. Anderson, and W. F. Stern, 1998: Reproducible forced modes in AGCM ensemble integrations and potential predictability of atmospheric seasonal variations in the extratropics. *J. Climate*, **11**, 2942–2959.
- Yasunari, T., 1980: A quasi-stationary appearance of the 30–40 day period in the cloudiness fluctuations during the summer monsoon over India. *J. Meteor. Soc. Japan.*, **58**, 336–354.
- Zebiak, S. E., 1989: On the 30–60 day oscillation and the prediction of El Niño. *J. Climate*, **2**, 1381–1387.